

Simulation of renewable feed-in for power system studies

Alexander Kies, Kabitri Chattopadhyay, Elke Lorenz,
Lüder von Bremen, Detlev Heinemann

Institute of Physics, University of Oldenburg

June 3, 2016

To investigate power systems with large share of renewables, it is important to understand the underlying weather-dependent feed-in patterns with high accuracy. In this report we describe how a highly resolved long-term weather data set was produced and used to calculate feed-in from different renewable sources like wind, photovoltaics and hydro within the framework of the RESTORE 2050 project. In particular, this report will provide an overview of the data sources, various assumptions that are made during the simulations and will present an elaborate description of the adopted methodology along with result evaluations. The RESTORE 2050 project investigates the needs for cross-country grid extensions, usage of storage technologies and capacities, wind and solar balancing potential and the conceptual design of the future European power systems. Since major renewable sources like wind and solar have strongly weather-dependent fluctuating feed-in profiles, a proper understanding of the balancing potential between their feed-in and the power demand is essential for their grid integration.



GEFÖRDERT VOM



Bundesministerium
für Bildung
und Forschung

Contents

1	Introduction	8
2	Overview on data and model	9
2.1	Meteo model	9
2.1.1	Downscaling of wind data	9
2.1.2	Solar irradiance retrieval for solar energy applications	12
2.1.3	Runoff data	15
2.2	Capacity distribution model	15
2.2.1	Country-level capacity distribution	15
2.2.2	Country Capacity Distribution	16
2.3	Power model	20
2.3.1	Wind power model	20
2.3.2	PV power model	22
2.3.3	CSP power model	23
2.3.4	Hydro power model	24
3	Analysis and Discussion	25
3.1	Validation	25
3.1.1	Validation of PV feed-in	25
3.1.2	Validation of CSP feed-in	28
3.1.3	Validation of Hydro inflow	31
3.2	Representative year analysis	32
3.2.1	Interannual variation of capacity factor	33
3.2.2	Interannual fluctuation of standard deviations	33
3.2.3	Application of Kolmogorov-Smirnov integral (KSI)	35
3.2.4	Analysis of incremental power time-series	36
3.2.5	Application of hypothesis testing	36
3.3	Spatio-temporal variability analysis	37
3.4	Comparison of statistical downscaling with dynamical downscaling	42
3.5	Dependency of the feed-in from wind on hub height and power curve	52
4	Summary and outlook	57
A	Appendix	58
A.1	Application of Kolmogorov-Smirnov integral	58
A.2	Hypothesis test	58
A.3	Concentrated Solar Power (CSP) in North Africa	59
A.3.1	Data set for North Africa	59
A.3.2	Cloud index data base	60
A.3.3	CSP in Spain and North Africa	62

List of Figures

1	Schematic flowchart and inter-connections between three different models (meteorological model, capacity distribution model and the power-generation model) used in this study for (1a) PV and (1b) wind.	10
2	Optimum inclination of the PV modules for a maximum annual yield (©IES, JRC).	14
3	Regional coverage of four transmission system operators over Germany . .	17
4	Resource-dependent distribution functions for Germany as applied for capacity distribution within country. Cumulated capacity distribution as a function of irradiance shown for two years and the same function for PV and wind which is applied for all years and all countries.	17
5	Installed wind power generation capacities in [MW] per grid cell (ISI-B scenario). The offshore areas show the average density of the corresponding offshore region.	18
6	Capacity factors calculated from COSMO-EU wind speeds with the Enercon E-126 power curve on the 7×7 km COSMO-EU grid for the year 2012 at 100m height.	18
7	Mean <i>DNI</i> for Spain (2003-2012) in $kWh/m^2/y$. Black dots mark CSP plants in operation in 2012 (left) and modelled for 2050 (right).	19
8	Power curves of the Enercon E-126 and an Enercon E-82/Vestas V-90. The lines without symbols indicate the theoretical limit of power output for both turbines.	20
9	Power curves of the Enercon E-126 (red), the average of the Enercon E-82 and the Vestas V-90 (blue) and the regional power curve developed in the Tradewind project (green).	21
10	Daily hydro inflow for the whole investigated regions for the years 2002-2003. .	24
11	Validation of normalised daily PV feedin with measurements for Germany, 2012	25
12	Hourly (top) and daily (bottom) comparison of PV simulations using 2050 (left) and 2012 (right) module configurations with upscaled measurements for Germany, 2012	26
13	European map of average annual sum (April, 2004 - March, 2010) of global horizontal irradiance from SolarGIS (left) (SolarGIS©2011 GeoModel Solar) and our simulation (right)	28
14	European map of average annual sum (April, 2004 - March, 2010) of global irradiance on inclined surfaces from European Union Joint Research Centre (EU-JRC) (left) (PVGIS ©European Union, 2001-2012) and our simulation (right)	29
15	Average annual sum of DNI in Spain from SolarGIS database (left) (SolarGIS©2013 GeoModel Solar) and our simulation (right)	30
16	Comparison of daily GHI (left) and daily DNI (right) time-series of 2006 in Almeria, Spain from SolarGIS database and our simulation	31

17	Monthly measured inflow of energy into hydro power plants and simulated inflow from reanalysis data for Norway.	32
18	Interannual variations of Europe's capacity factors for different renewable resources.	34
19	Ratio of standard deviation of power to the standard deviation of the reference time-series for different technologies in Europe.	35
20	Interannual variation of KSI at different temporal resolutions. Distance between the distribution of annual power generation and the ten years reference time-series is expressed as the KSI values.	36
21	Distribution of the increments of power in relation to the increments of the ten years reference time-series expressed as the KSI to analyse interannual variations of KSI at different temporal resolutions.	37
22	The strong deterministic effect of the sharp gradient associated with diurnal solar course	38
23	KSI test results for hourly and daily normalised power time-series at 95% confidence level	38
24	Yearly mean (left) and yearly standard deviation (right) maps of PV capacity factor for Europe calculated over ten years (2003-2012).	39
25	Interannual variation of weekly time-series of PV and wind for Germany .	39
26	Weekly PV, wind and hydro time-series for Germany during 2004	40
27	PV, offshore and onshore wind power productions for ten days in January (left) and ten days in July (right), in 2004 for Germany	40
28	Diurnal variation of average load, PV and wind power for Germany	41
29	Cumulated distribution (left) and incremental cumulated distribution (right) of hourly (top panel), daily (middle panel) and weekly (bottom panel) PV and wind power for Germany	42
30	Cumulated distribution of hourly normalised PV (left) and wind (right) for Europe, Germany and Spain	43
31	Interannual variation of (31a) PV and (31b) wind capacity factors for European countries, arranged in ascending order of ten years average . . .	44
32	Average wind speeds in [m/s] from the COSMO-EU analysis model for the investigated domain for the comparison of statistical and dynamical downscaling at 140 m height for February to November 2009..	45
33	Average wind speeds in [m/s] from the stat downscaling (top) and dynamical downscaling (bottom) at 140 m height for February to November 2009.	46
34	Correlation coefficients for the investigated domain per grid cell for February until November 2009 between COSMO-EU wind speeds and statistically downscaled wind speeds at 50 m height (top) and 140 m height (bottom).	48
35	Correlation coefficients for the investigated domain per grid cell for February until November 2009 between COSMO-EU wind speeds and dynamically downscaled wind speeds at 140 m height.	49

36	Rmse for the investigated domain per grid cell for February until November 2009 between COSMO-EU wind speeds and statistically downscaled wind speeds at 50 m height (top) and 140 m height (bottom).	50
37	Rmse for the investigated domain per grid cell for February until November 2009 between COSMO-EU wind speeds and dynamically downscaled wind speeds at 140 m height.	51
38	Weekly capacity factor [%] for wind computed applying the Enercon E-126 power curve to COSMO-EU wind speeds in the year 2012 for three different hub heights for Germany.	53
39	Weekly capacity factor[%] for wind computed using COSMO-EU wind speeds for the year 2012 for two different power curves at 100 m hub height. The red feed-in was computed for an Enercon E-126 power curve and the blue line for the average of the Enercon E-82 and the Vestas V-90 power curve.	54
40	Correlation factors for every country investigated onshore between the time series computed with the Enercon E-126 power curve and one half the Enercon E-82 and Vestas V90 power curve for the year 2012 from COSMO-EU wind speeds in 140 m height.	55
41	Correlation factors for every country investigated offshore between the time series computed with the Enercon E-126 power curve and one half the Enercon E-82 and Vestas V90 power curve for the year 2012 from COSMO-EU wind speeds in 140 m height.	56
42	Illustration of Kolmogorov-Smirnov statistics	58
43	Diurnal cycles of <i>DNI</i> using respective algorithms for MFG and MSG for an example day in 2005 averaged over the entire model domain of North Africa. The figure shows improvements achieved upon quality control of satellite images.	61
44	Diurnal cycles of <i>DNI</i> using respective algorithms for MFG and MSG for a few days in 2005 averaged over the model domain of North Africa. The figure represents the result of model adaptation to be more suitable to the narrowband channel.	61
45	Improvement upon quality control of MSG, shown for hourly (left) and daily (right) time-series for North Africa during 2005.	62
46	Daily time series of CSP power normalised to installed capacities during 2012 for Spain and North Africa.	62
47	Inter-annual variation of CSP capacity factor for Europe and North Africa.	63

List of Tables

1	Module configurations as adopted from the ISI meta study [17]	14
2	Adaptation of country-level CSP capacities (GW) from EWI energynautics report [8] to that of meta-study ISI [17].	16
3	List of variables related to CSP power calculation	23
4	Overview of results from hourly PV time-series of 2012 for Germany . . .	26
5	Comparison between normalised PV power with 2012 and 2050 module configurations using upscaled measurements for Germany, 2012	27
6	Overview of Andasol and Vally CSP power plants' performances and comparison with our simulations for 2012 at nearest grid point of the model domain	31
7	Average wind speeds and standard deviations for the three compared wind speed models in the whole covered domain for February until November 2009 at 140 m height.	47
8	Root mean square differences and correlation coefficients for the three models pairwise computed for February until November 2009 as used for comparison and verification.	47
9	Feed-in for Germany for February until November 2009 calculated with the Enercon E-126 power curve from the three different wind speed models at 140 m hub height. Mean and Standard deviation are for hourly capacity factors.	52
10	Correlation coefficients between the hourly feed-in time series' calculated from the three different wind speed models for Germany with the Enercon E-126 power curve at 140 m hub height for February until November 2009. .	52
11	Statistical measures to compare CSP production and variability between Europe and North Africa (standard deviation normalised to mean power, gross annual production for 81GW installed capacity for both Europe and North Africa & standard deviation of hourly time series).	63

1. Introduction

The project RESTORE 2050 by Next Energy, University of Oldenburg and the Wuppertal Institute investigates the transformation towards a reliable power system for European countries in 2050 based on high shares of renewable generation. The weather-dependent nature of major renewable sources like solar and wind causes renewable feed-in to have highly fluctuating patterns. The integration of the intermittent nature of renewable generation into the power system is a challenging task. Different solutions were proposed in the past to overcome the generation-consumption mismatch problem like excess generation [10] or transmission grid extensions [2]. A combination of these options seems to be the most realistic way to operate a highly renewable power system.

For the RESTORE 2050 project, feed-in time series of renewables are the basis of the power system simulations. Hence, 10-year time series (2003-2012) of different renewable feed-in are generated from different data sources, including satellite data and the results of numerical weather prediction (NWP) models. The feed-in data is generated at high spatial (7×7 km) and temporal (hourly) resolutions. In this report we discuss the meteorological data and the model description to obtain feed-in time series on grid point and country-level from the raw data. The basic steps are:

- meteorological assessing raw data (e.g. wind speeds from NWP models, irradiance from satellite data)
- pre-processing the raw input data in usable form (i.e. extrapolation of wind speeds to the desired height, converting global horizontal irradiance on inclined surfaces)
- converting the weather data (e.g. irradiation, wind speed) to power
- aggregating the feed-in power to the country-level

Renewable deployment scenarios

Two scenarios for renewable deployment are chosen for the RESTORE 2050 project. One is scenario b of the study “Tangible ways towards climate protection in the European Union (EU Long-term scenarios 2050)” [17] published by Fraunhofer ISI in 2011. The second is the energy revolution scenario of energy “[r]evolution - A SUSTAINABLE EU 27 ENERGY OUTLOOK” [9] published by EREC in 2012. Some assumptions from these scenarios are used:

- a) The installed renewable generation capacities of single countries in 2050
- b) PV module configurations for pv power calculations

Additionally, the scenario from meta study ”Roadmap 2050 - a closer look” [8], published in 2011, is used for the country-level capacity distribution of CSP.

2. Overview on data and model

This section gives an overview of the meteorological data and models used in this work. For both PV and wind, three different models are used to compute the country-level feed-in time series. These are the meteo model, the capacity distribution model and the power model (Fig. 1).

The simulation of PV power requires irradiance and temperature while wind power simulation needs wind speed as model input. For hydro power calculations runoff data is required.

2.1. Meteo model

A large weather data base is produced to simulate feed-in with the desired spatial and temporal resolution for 34 European countries. This section describes the data used and the applied methods.

2.1.1. Downscaling of wind data

To simulate feed-in from wind power, detailed temporal and spatial knowledge of the wind speed field is necessary. This is obtained by a numerical weather prediction (NWP) model. A 7×7 km spatial resolution and hourly temporal resolution was chosen to be sufficient for feed-in simulation purposes within the RESTORE 2050 project. The COSMO-EU NWP model has the desired resolution. However, it does not date back to 2003, therefore MERRA Reanalysis data [19] was chosen instead. MERRA reanalysis provides wind speeds in 10 and 50 m height from 1979 onwards at a spatial resolution of $2/3 \times 1/2$ degrees and a hourly temporal resolution. To obtain a finer resolution MERRA wind speeds were statistically downsampled to the 7×7 km grid. The downscaling process consists of three steps, that are being described in more detail here. In addition the 2 m temperatures used for the calculation of pv power were also taken from the MERRA reanalysis and are downsampled to the COSMO-EU grid.

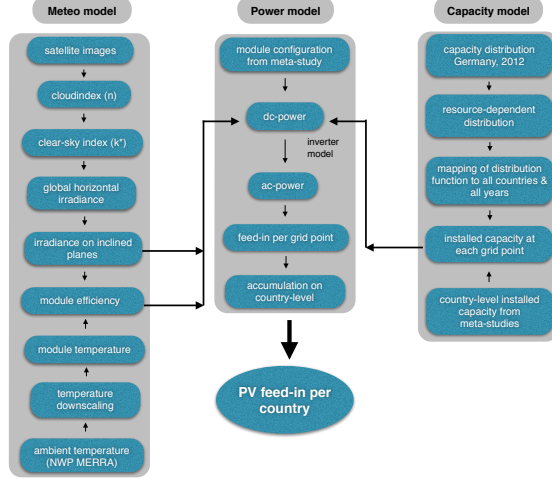
2.1.1.1 Horizontal Interpolation

To increase spatial resolution of the wind speeds and temperatures a spatial interpolation was performed using an approach with interpolation weights being inverse distances squared and taking 8 nearest neighbours into account according to

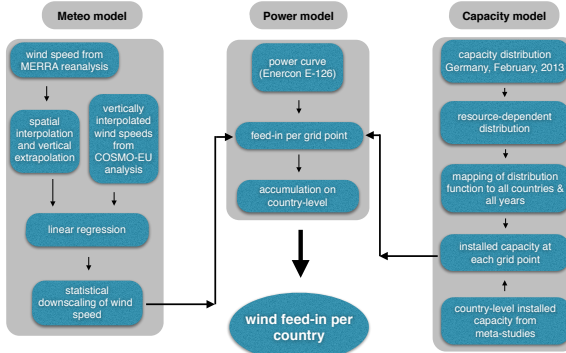
$$u(x) = \frac{\sum w_i u_i(x)}{\sum w_i}$$

with $u_i(x)$ being the $i \in [1, n]$ datapoints given, $u(x) : x \rightarrow \mathbb{R}, x \in D \subset \mathbb{R}^2$ being the expected result for wind speed components or temperature and the weights w_i given by

$$w_i(x) = \frac{1}{d^2(x, x_i)},$$



(a) PV flowchart



(b) wind flowchart

Figure 1: Schematic flowchart and inter-connections between three different models (meteorological model, capacity distribution model and the power-generation model) used in this study for (1a) PV and (1b) wind.

d being the Euclidean metric. After the interpolation was performed, the wind speed components are available on the COSMO-EU grid. At this point, the wind speed at every single grid point was computed from the wind speed components u, v according to

$$s = \sqrt{u^2 + v^2},$$

which is the simple vector norm.

2.1.1.2 Vertical extrapolation

Wind speeds are given from the MERRA reanalysis at a height of 50 m. To simulate power a hub height of 140 m was chosen (section 2.3.1.1 for details). To extrapolate the given wind speeds to the desired height after interpolation the log wind profile was assumed to yield reliable results. The log wind profile is a semi empirical relationship used to describe the relationship between wind and height in the lowest part of the planetary boundary layer. Wind speeds near ground are mainly influenced by the roughness length. The profile is given implicitly by

$$\frac{s(z)}{s(z_r)} = \frac{\log(z/z_0)}{\log(z_r/z_0)},$$

where $s(z)$ is the velocity at height z , z is the desired height to be extrapolated to, z_0 is the height for which the velocity is available and z_r is the surface roughness length, which is the parameter to model the logarithmic wind profile. In the model it is obviously the height at which wind speeds become zero. Roughness lengths for the 7×7 km grid are taken from the COSMO-EU model and are used to extrapolate wind speeds. For the COSMO-EU wind speeds a linear height interpolation between the two neighbouring model levels of 140 m height is done to perform the linear regression in the next step.

2.1.1.3 Linear regression

In the final downscaling step a linear regression between the vertically extrapolated wind speeds from MERRA on the 7×7 km grid at 140 m height and the COSMO-EU wind speeds is performed. Regression coefficients are being calculated for the year 2012 and then applied for all ten years 2003-2012. The relationship between COSMO-EU wind speeds S_c and MERRA wind speeds S_m (both on the same grid and at the same height) is assumed to be

$$S_c = \epsilon + xS_m,$$

with ϵ and x being the coefficients of the linear regression. These coefficients are calculated by the method of least squares and the resulting coefficients are then applied on the MERRA Reanalysis data to yield the final wind speeds on a 7×7 km grid at a height of 140 m. The assumption here is that COSMO EU wind speeds yield more reliable results than MERRA reanalysis wind speeds since they are computed at a finer resolution. Later in this report (Sec. 3.4) this statistical regression is compared with a dynamical WRF (Weather Research Forecast) simulation.

2.1.2. Solar irradiance retrieval for solar energy applications

For solar power calculation, irradiance can either be collected from ground measurements or calculated from numerical models or retrieved from satellite data. For this work, we have used Meteosat satellite images to obtain solar irradiance. One of the advantages of using satellite data over ground measurements is that satellites can provide near-continuous spatial coverage with high temporal resolution, which is ideal for analysing large domains where measurements may be sparse in space and time.

2.1.2.1 Solar irradiance from satellite images

Images from geostationary satellites can provide valuable information on cloud cover and solar irradiance with continuous spatial coverage. Irradiance retrieval is influenced by the deterministic daily course of the sun as well as the variable meteorological effects, especially the cloud cover. In this work, the deterministic effect is modelled with a clear sky model while the cloud information is derived from satellite images. Here we have used the Heliosat method [5] to derive surface solar irradiance from Meteosat images. This method is driven by the fact that usually the albedo of the earth's land and ocean surfaces is smaller than that of a cloudy atmosphere. Hence, higher planetary albedo is expected for cloudy situations compared to clear sky conditions.

The Heliosat method provides information on cloud transmittance using albedo data measured by geostationary satellites. This method consists of three steps. In the first step a statistical analysis is carried out on a time-series of reflectance values to identify clear sky time slots for each image pixel and to determine the ground albedo (ρ_g). In the next step, the cloud index (n) is computed using:

$$n = \frac{\rho - \rho_g}{\rho_o - \rho_g},$$

where ρ is the actual albedo and ρ_o is the same for overcast conditions. Cloud index values close to 0 represent clearsky conditions while values close to 1 indicate overcast conditions. Intermediate cloud index values represent broken cloud or semitransparent cloud conditions.

At this point, it is important to introduce the clear-sky index (k^*) which is used as a measure of atmospheric extinction:

$$k^* = \frac{GHI}{I_{clear}}, \quad (1)$$

where GHI is the global horizontal irradiance and I_{clear} is the same under clear-sky conditions. I_{clear} is derived from a clear-sky model which requires solar elevation and atmospheric turbidity as input parameters. For this work, we have used turbidity according to [4] and the clear-sky model from [16].

The third, and the final step of the Heliosat method is to derive the clear-sky index from an empirical relationship with cloud index (n):

$$k^* = 1 - n$$

Once k^* is calculated from cloud index and I_{clear} is obtained from the clear-sky model, it is possible to determine global horizontal irradiance from equation (1).

Different generations of Meteosat satellites were operational during different periods of our simulation (2003-2012). These satellites from different generations have different spatio-temporal resolutions. For 2003-2004, irradiance data from Meteosat First Generation (MFG) satellites were used. We chose the broadband visible channel (VIS) of MFG which has a spectral range of $0.5 - 0.9\mu m$ and is the most suitable one for cloud detection. This channel has a spatial resolution of 2.5×2.5 km at sub satellite point and collects data every 30 minutes. The remaining years are simulated with irradiance from Meteosat Second Generation (MSG) satellites. MSG has one high resolution visible (HRV) channel with an improved sampling interval of 15 minutes and a 1×1 km spatial resolution at the sub-satellite point. We used irradiance retrieved by this broadband HRV channel of MSG for 2005-2012. This channel operates over the spectral range of $0.6 - 0.9\mu m$. To maintain uniformity with wind, all data are regridded to 7×7 km resolution and averaged to hourly resolutions.

2.1.2.2 Solar irradiance on tilted PV modules (Plane-of-array irradiance)

The power output from solar PV modules is significantly affected by their orientation given by azimuth and tilt angle. These two parameters change the amount of solar irradiance received on PV modules and hence alter power output. The optimum tilt angle of a module at a certain location under clear sky condition is typically close to its local latitude. Hence, with increasing latitude, PV power for clear sky conditions can be optimised by increasing module inclinations. However, the situation is quite different for overcast or broken cloud conditions. During cloudy situations, most irradiance is diffuse as clouds hinder the direct sunlight. In this case, large tilt angles of the PV modules result in a significant loss of power due to the ‘shading’ of most of the diffuse radiation. Hence, for all practical purposes, the optimum tilt angles are kept at a lower angle than the local latitude. For this study, the optimum tilt angles for each country are chosen from the map (shown in Fig. 2) provided by IES, the European Commission’s Joint Research Centre (JRC) [11].

The configurations of the PV modules are adopted from the ISI meta study [17]. Table 1 summarises the relative contributions of different tilt angles and module azimuth angles. Since our model domain covers selected regions in the northern hemisphere, the most suitable module configuration would be optimally inclined south-facing modules. However, especially smaller PV systems (e.g. roof-top PV) are often not oriented in an optimized manner. So, to keep our assumptions realistic, three different orientations (south-east, south, south-west) and five different tilt angles are proposed. The relative contributions of these configurations to the final power production is quite different from each other and is taken from [17], see table 1. The ISI study [17] does not include

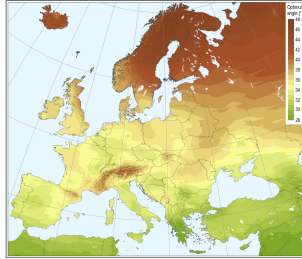


Figure 2: Optimum inclination of the PV modules for a maximum annual yield
©IES, JRC.

any tracking configuration and to keep our assumptions close to these meta-studies, the tracking option has been omitted in our work as well.

Parameter	Configuration	Share
Tilt angles	-10°	5%
	-5°	20%
	Opt. angle	50%
	5°	20%
	10°	5%
Orientation	south-east	20%
	south	60%
	south-west	20%

Table 1: Module configurations as adopted from the ISI meta study [17]

The conversion of global horizontal irradiance on inclined surfaces is based on the Klucher model [14].

2.1.2.3 Direct normal irradiance calculation for CSP

Direct Normal Irradiance (DNI) is the direct solar irradiance component received by a surface oriented perpendicular to the direction of the sun.

$$DNI = \frac{I_{dir}}{\cos \theta_z},$$

where I_{dir} is the direct irradiance component on the horizontal plane and θ_z is the solar zenith angle. The direct component is computed by subtracting the diffuse part I_{diff} from global horizontal irradiance GHI . Hence, DNI can also be written as:

$$DNI = \frac{GHI - I_{diff}}{\cos \theta_z}.$$

DNI is highly variable in space and time, and so is the PV power. Decreasing *DNI* may be caused by a number of factors, including cloud coverage, presence of water vapor and aerosols in the atmosphere.

2.1.3. Runoff data

Hydropower has been calculated from ERA-Interim [6] run off data at a spatial resolution of ca. 70×70 km with a daily temporal resolution. Runoff is precipitation minus evaporation minus soil infiltration. In the verification section it is shown that it is possible to reproduce seasonal patterns of inflow into storages at least for Norway.

2.2. Capacity distribution model

The capacity distribution model used in RESTORE 2050 has two major components. The first one deals with the country-level capacity of different renewables while the later concerns with capacity distribution within each country.

2.2.1. Country-level capacity distribution

For RESTORE 2050, country-level capacities are taken from two existing scenarios with high shares of renewable energy supply in Europe. Both scenarios have a renewable penetration close to 100% in the year 2050. The capacity values in both of these studies are given for almost all investigated countries. for EU-27 or EU-27 + CH/EU. Missing capacity values for the Balkan countries are derived under the assumption that the area weighted capacity values of the surrounding countries like Bulgaria, Greece, Hungary, Romania and Slovenia, also holds true for the Balkan countries by 2050. For Norway, capacities were estimated internally.

By including the additional countries in our simulation, we slightly modify the total installed capacity for Europe. After this modification, the ISI-scenario projects that by the year 2050, Europe's onshore and offshore wind capacities will reach roughly 620.0 GW and 212.3 GW, respectively. On the other hand, the inclusion of Balkan countries cause EREC scenario to estimate roughly 317.7 GW and 206.8 GW capacities for onshore and offshore winds. Both scenarios have a similar share of offshore wind capacity but the ratio of PV and wind onshore is very different from each other. While ISI-scenario projects roughly a 1:2 ratio for PV and onshore wind, EREC-scenario depicts almost 2:1 ratio for the same. For solar PV, the projected capacity for Europe, including the Balkan countries, is 340.5 GW for ISI and 614.3 GW for EREC.

For CSP, ISI and EREC project 18 GW and 81 GW installed capacity for Europe, respectively. However, country-level capacity values for CSP are not given in these two meta-studies. For ISI scenario, the country-level capacity values are given in combination with other renewables like wave, geothermal, tidal etc. Hence, the country-level capacity values for CSP were adopted from the EWI energynautics report [8] and scaled-up to match the aggregated installed capacity for Europe as given by ISI and EREC respectively. The actual and scaled CSP capacity values are summarised in table 2.

Since CSP plants depend on the direct component of solar irradiance, regions with poor irradiance (either due to geographical reason or as a result of frequent cloud cover) are not suitable for constructing CSP plants. According to the meta study EWI [8], only Spain, Italy and Greece will have CSP plants by 2050. These countries are located in the southern part of Europe where there is sufficient direct sunlight available throughout the year and conclusively are quite suitable for building CSP plants. Hence, only these three countries are investigated in RESTORE 2050 project for feed-in from CSP plants.

Countries	EWI	Scaled with ISI	Cumulated with other renewables (ISI-scenario-B)
Spain	108.9	9.9	15.0
Italy	70.2	6.4	7.5
Greece	19.0	1.7	2.2

Table 2: Adaptation of country-level CSP capacities (GW) from EWI energynautics report [8] to that of meta-study ISI [17].

2.2.2. Country Capacity Distribution

2.2.2.1 PV and Wind

For the capacity distribution of PV and wind generation facilities within single countries, an empirically resource-dependent distribution is applied. This is based on the real distribution in one of the recent years (2012 for PV and 2013 for wind). Detailed information on the capacity distributions in all countries is not available to us for all investigated countries. Germany is currently one of the countries with highest installed PV and wind power capacities in Europe. Consequently, we assume that its installations might be representative for Europe in the midterm-future (2050). Thus, its resource-dependent distribution might be a realistic way to model the future European PV and wind power generation deployment. Our approach consists of the following steps: the relationship between average resource and installed capacity per grid cell with a spatial resolution of 7×7 km is derived for Germany based on available data as for 2012 for PV and February 2013 for wind. For Germany, PV installed capacities are provided by four transmission system operators (TSO), namely, 50 Hertz, Amprion, Tennet and Transnet-BW (Fig. 3).

The capacity distribution within country is modelled for Germany from the empirically derived relationships shown in Fig.4b. This function is later transferred to all investigated countries. For every other country the German grid cells on the x-axis of Fig. 4b are replaced by the respective grid cells of the country.

The curves shown in figure 4a represent the irradiance-dependent PV capacity distribution functions for two years, 2008 and 2012. Since the locations with best available irradiance are filled up first, the curve of 2008 is quite steep in the beginning. With time, other locations with comparatively poor resources are also filled up and this effect is reflected in the curve of 2012.



Figure 3: Regional coverage of four transmission system operators over Germany

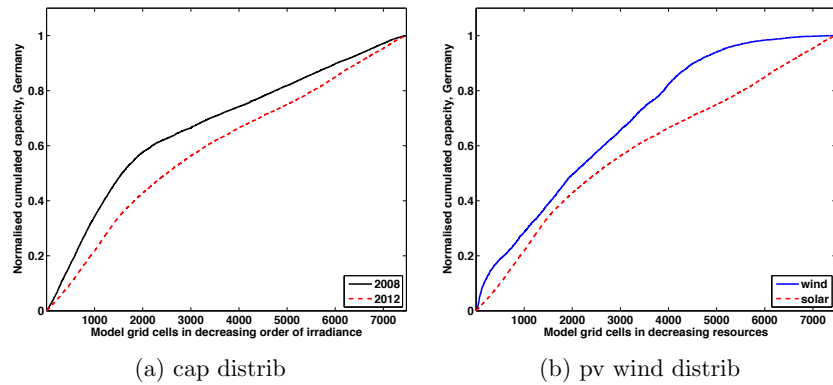


Figure 4: Resource-dependent distribution functions for Germany as applied for capacity distribution within country. Cumulated capacity distribution as a function of irradiance shown for two years and the same function for PV and wind which is applied for all years and all countries.

Usually Capacity factors for offshore wind turbines increase with increasing distance from the coast line. However, with increasing distance to the coast investment cost rises as well. Because it remains unclear, which factor will be more prominent by 2050, a simple approach is chosen: For offshore the general distribution curve is kept, but grid cells are randomly chosen. This leads to an inhomogenous capacity distribution disregarding any resources dependency. The resulting distribution of wind capacities is shown in Fig. 5. Onshore the installed wind capacity in [MW] is shown for every grid cell of 7×7 km while offshore only the average density of the offshore region belonging to the corresponding country is shown. Like expected the modelling approach leads to high densities of installed capacities in regions where capacity factors are highest such as the coastal regions of Germany, Poland and France, the UK and Denmark. Offshore the highest densities occur for Germany and the Netherlands due to the very small offshore

areas in comparison to the very high expected installed offshore capacities in 2050 by the ISI-scenario.

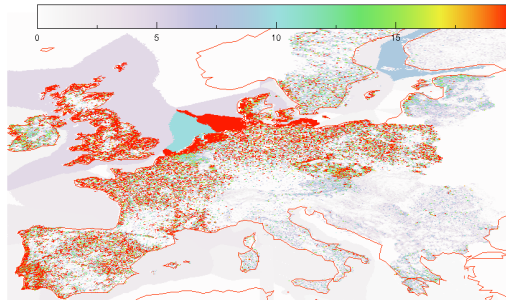


Figure 5: Installed wind power generation capacities in [MW] per grid cell (ISI-B scenario). The offshore areas show the average density of the corresponding offshore region.

Fig. 6 shows the wind capacity factors for the used 7×7 km grid computed for 2012 with the Enercon E-126 power curve at 100 m hub height and the COSMO-EU wind speeds. The capacity factors describe the average yield of power over the nameplate capacity. These values are highest in the offshore regions reaching around 0.6. Onshore the highest capacity factors are reached in the coastal regions of the northern and middle-european countries with values of around 0.4. The lowest capacity factors of in some parts less than 0.1 are in the south east of Europe, so mainly the Balkan countries and Greece. As can be seen from the figure there is a strong Northwest-Southeast slope in the capacity factors. The approach, that is described in this section, is used to distribute capacities within the single countries.

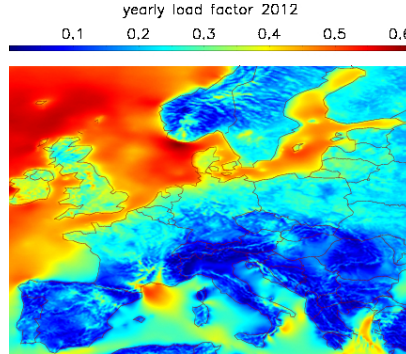


Figure 6: Capacity factors calculated from COSMO-EU wind speeds with the Enercon E-126 power curve on the 7×7 km COSMO-EU grid for the year 2012 at 100m height.

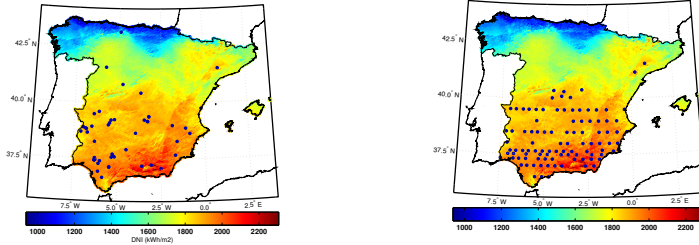


Figure 7: Mean DNI for Spain (2003-2012) in $kWh/m^2/y$. Black dots mark CSP plants in operation in 2012 (left) and modelled for 2050 (right).

2.2.2.2 Inner country CSP distribution

Unlike solar PV, the number of CSP plants installed today in Europe is very low. This limits the use of a resource dependent distribution function to be applied for CSP. Nevertheless, it is extremely important to include the resource dependency for CSP distribution as the energy yield strongly depends on the direct component of solar radiation. Hence, in RESTORE 2050, we have chosen the best locations for CSP plants according to the average DNI maps (Fig. 7). A CSP plant needs to have at least a minimum of average DNI available for proper performance, both technically and economically. According to DLR [21], this threshold is $1800\text{ }kWh/m^2$ per year for technical potential and $2000\text{ }kWh/m^2$ per year for economic potential. Hence, in our model, a threshold of $1800\text{ }kWh/m^2$ of DNI is used to select the best locations for CSP installation. However, this threshold is quite inadequate to implement a large number of CSP plants in Italy and Greece where the average annual DNI rarely reaches this threshold. So, a lower threshold of $1750\text{ }kWh/m^2$ per year is used for Italy and Greece. For Spain, however, the original threshold of $1800\text{ }kWh/m^2$ per year is used as it works well for this country. The distribution of Spanish CSP plants operational in 2012 and the CSP plants implemented in our model for 2050 is shown in Fig. 7.

According to [23], most CSP plants currently operational in Spain have 50 MW capacity. There are also a few larger CSP plants of 100 MW capacity currently operational in Spain. Assuming reasonable development in CSP technology and the expanded market by 2050, we have used CSP plants with 100 MW capacity in our simulations.

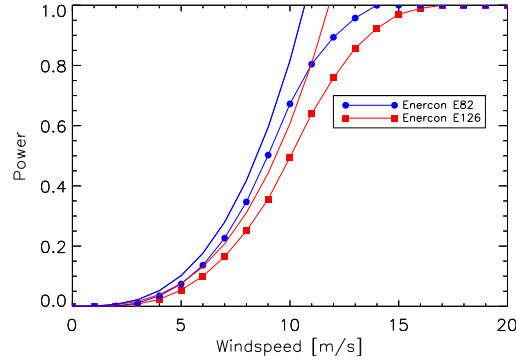


Figure 8: Power curves of the Enercon E-126 and an Enercon E-82/Vestas V-90. The lines without symbols indicate the theoretical limit of power output for both turbines.

2.3. Power model

This section describes how wind speeds, irradiance etc. are converted to power for the corresponding technologies.

First, the power output is calculated for every grid cell. In a following step the grid cells of each country are aggregated to the country level.

2.3.1. Wind power model

This section describes how the wind feed-in time series was calculated. The wind speed data that has been used was described in Sec. 2.1.1. Wind energy is the energy extracted from the kinetic energy of the wind by the use of a wind turbine. So the generated power of a wind turbine is a function of the kinetic energy of the mass flow through its swept area

$$P = \eta \frac{\dot{m}v^2}{2} \\ = \eta \frac{\rho A v^3}{2},$$

where η is the overall efficiency of the whole process, \dot{m} is the mass flow rate, A is the swept area, ρ the density of air and v the wind speed. Figure 8 shows the power curves of two wind turbines, that were compared in a later section and their theoretical limits using the efficiency $\eta_B = 16/27$. η_B is the Betz limit that defines the theoretical maximum of efficiency in an open disk actuator modelling approach.

2.3.1.1 Power curve

In principle it would be possible to take the power of the wind directly as power output. However, the efficiency of a wind power converter is not constant but a function of wind

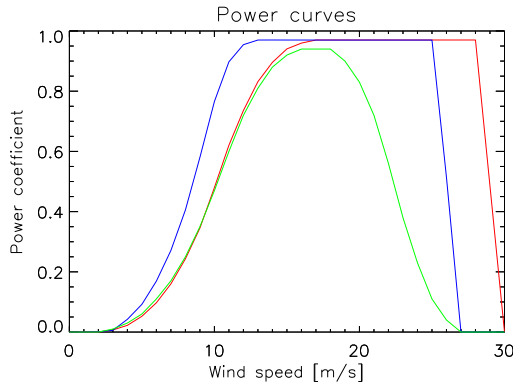


Figure 9: Power curves of the Enercon E-126 (red), the average of the Enercon E-82 and the Vestas V-90 (blue) and the regional power curve developed in the Tradewind project (green).

speed with some characteristics. For low wind speeds the torque exerted by the wind on the blades of the turbine is too low to generate angular momentum. The wind speed at which the blades start to rotate and therefore produce power is called the cut-in speed of a turbine. These cut-in speeds are usually below 5 m/s. When the wind speed exceeds the cut-in speed the power output of the generator increases rapidly and resembles the v^3 dependency of the kinetic energy passing through the swept area. At about 10 m/s the turbine efficiency starts to decrease and at the rated wind speed of about 15 m/s the turbine reaches maximal power output that is constant with increasing wind speeds. One common way to obtain this constant energy output is the adjustment of the blade angles to keep the power at a constant level (pitching). With further rising wind speeds forces exerted on the turbine increase further and are able to cause structural damage to the rotor. At this cut-out wind speed (Roughly between 25 and 30 m/s) the rotors are stopped.

The Enercon E-126 is the chosen turbine to model the wind power time series within the RESTORE 2050 project onshore and offshore. It is a wind turbine model manufactured by Enercon with a hub height of 135 m, a rotor diameter of 127 m and a nameplate capacity of 7.58 MW, making it one of the largest commercially available wind power turbines in the year 2014.

It's manufacturers power curve was taken and modified by 5% plain losses to account for electrical losses, wake effects etc. to model the wind feed-in time series. In section 3.5 the feed-in calculated with this power curve is compared with the feed-in calculated with the average power curve of the Enercon E82 and the Vestas V90, which is supposed to be close to the average of new installations in Germany around 2013.

2.3.2. PV power model

We have used a robust simulation model [15] to calculate the PV power output (P_{PV}) from irradiance received on inclined module surfaces (I_t). This model is suitable to compute power from a wide variety of module types, including the classic crystalline silicon and various other thin film technologies. So, we have selected this model for regional power calculation which, for all practical purposes, requires a variety of module types to be considered.

The first step of the PV power model is to estimate the efficiency (η_{MPP}) of PV generators operated in maximum power point (MPP) in dependence on irradiance of inclined planes (I_t) and the PV module temperature (T_m). The influence of irradiance on the module efficiency at temperature $T_m = 25^\circ C$ is expressed via a parametric model (Eqn. 2).

$$\eta_{MPP}(I_t, 25^\circ C) = a1 + a2 \times I_t + a3 \ln I_t \quad (2)$$

where $a1$, $a2$ and $a3$ are device-specific parameters and they are determined either from manufacturers' module data sheet information or from the measurements. They are in the range of 0.0220 to 0.0226, -0.00001870 to -0.00001876 and 0.0170 to 0.0178 for $a1$, $a2$ and $a3$ respectively. These parameters remain constant for all grid points throughout the model domain. Here we are interested in obtaining efficiency at module temperature, which may not always be $25^\circ C$. Hence, module performance at a general operating temperature T_m is modelled by the standard approach using a single temperature coefficient (α) (Eqn. 3). We have used a numerical value of -0.004 for α [3]. (ΔT_m) is the temperature difference between the module temperature and the standard $25^\circ C$.

$$\eta_{MPP}(I_t, T_m) = \eta_{MPP}(I_t, 25^\circ C)(1 + \alpha \Delta T_m) \quad (3)$$

Since high module temperature usually indicates poor efficiency of the model, α values are generally negative. Heating of the module can be quantified by using irradiance and ambient temperature as input (Eqn. 4). The parameter γ is determined by the mounting type of the system. For example, roof top PV modules are usually heated up faster than the individual stand-alone systems. Hence the γ values for the former ($0.056^\circ C m^2/W$) are larger than the later ($0.02^\circ C m^2/W$). We have used a numerical value of 0.036 for γ to have a very generalized model of Europe with wide variety of PV mounting systems [3].

$$T_m = T_a + \gamma I_t \quad (4)$$

With all the above information on module efficiency, module temperature and incoming irradiance on the inclined planes, it is possible to calculate the power output (P_{PV}) from a PV generator (Eqn. 5).